2023-01-31

Kinematic/static model of complex compliant mechanisms with serial-parallel substructures: a general approach

Mingxiang Ling

Junyi Cao

Larry L. Howell
Brigham Young University - Provo, lhowell@byu.edu

Original Publication Citation

"Ling, M., Cao, J. Howell, L.L., Zeng, M., “Kinetostatic Modeling of Complex Compliant Mechanisms with Serial-Parallel Substructures: A Semi-Analytical Matrix Displacement Method,” Mechanism and Machine Theory, Vol. 125, pp. 169-184, https://doi.org/10.1016/j.mechmachtheory.2018.03.014, 2018."

Kinematic/static model of complex compliant mechanisms with serial-parallel substructures: a general approach

Mingxiang Ling[a,b], Junyi Cao[1a], Larry L. Howell[c]
[a] State Key Laboratory for Manufacturing Systems Engineering, Xi'an Jiaotong University, Xi'an 710049, China
[b] Institute of Systems Engineering, China Academy of Engineering Physics, Mianyang 621999, China
[c] Department of Mechanical Engineering, Brigham Young University, Provo, Utah, 84602, USA

Abstract
Kinematic and static analyses of compliant mechanisms are crucial at the early stage of design, and it can be difficult and laborsome for complex configurations with distributed compliance. In this paper, a general and concise kinematic/static modeling method of flexure-hinge-based compliant mechanisms with arbitrary serial-parallel substructures is presented to provide accurate and efficient solutions by combining the matrix displacement method with the transfer matrix method. The transition between the elemental stiffness matrix and the transfer matrix of the flexure hinge and the flexible beam is straightforward, enabling the condensation of a hybrid serial-parallel substructure into one equivalent element simple. Then, the static model of the whole compliant mechanism can be easily established based on the equlibrium equation of the nodal force. The input/output force-displacement relations and the Jacobian matrix are further built for single-DOF and multi-DOF compliant mechanisms based on the modeling method. Comparison of the proposed method with finite element analysis and experiment for two exemplary mechanisms reveals good prediction accuracy, suggesting its feasibility for fast performance evaluation and parameter optimization at the initial stage of design.

Keywords: *Compliant mechanism; flexure hinge; flexible manipulator; transfer matrix method*

1. Introduction

Unlike traditional rigid-body mechanisms, compliant mechanisms transmit motion, force and energy through elastic deformations of their components. Compliant mechanisms can provide highly accurate smooth motions without wear, friction, backlash and often need no assemble [1]. Therefore, they have attracted widespread attentions in variety of scientific and industrial applications, including precision positioning, micro griping manipulation and precision manufacturing [2-5]. However, one of the disadvantages in comparison to conventional rigid-body mechanisms is that their design and analysis require simultaneous consideration of kinematic and elasto-mechanical behaviors.

Most compliant mechanisms are organized serially, in parallel or in their hybrid configurations with various kinds of flexure hinges. The kinematics, statics and dynamics of these flexure-hinge-based compliant mechanisms can be analyzed similar to multi-rigid-body mechanisms by modeling the flexure hinge as an equivalent joint with springs based on the pseudo-rigid-body model [1]. Serial compliant mechanisms can also be easily analyzed by employing the transfer matrix method or the chain algorithm [6]. However, for complex mechanisms with serial-parallel substructures and distributed/hybrid compliance, which are widely applied in engineering, the above mentioned modeling methods are incomplete and other methods are need.

Finite elemental analysis is one of the most popular methods for analyzing compliant mechanisms. It can provide excellent solutions for general structures with no constraint on geometry. However, the procedure is time consuming for frequent iterations at the early stage

[1] Corresponding author Email: caojy@mail.xjtu.edu.cn

of design where many concepts should be evaluated in a short period of time. Meanwhile, a sufficiently large number of elements are inevitable for flexure hinges to obtain a reliable result. Thus, it requires too much time to be feasible for fast performance prediction and real-time controller design, though it is often used to verify performance before fabrication.

Considering the limitations of FEM, theoretical modeling for compliant mechanisms has been an interesting and hot issue since the pioneer works of analytical modeling for flexure hinges by Paros and Weisbord [7] and the subsequent works by Howell, Lobontiu and other scholars [1, 8]. Many theoretical methods are now available such as the pseudo-rigid-body model (PRBM) [5], the elastic beam theory [9, 10], the Castigliano's second theorem [11, 12] and the compliance matrix method [13, 14]. PRBM was proposed to solve the problem of large deformations [1, 15-17] and now it is also used for kinematic and static modeling of compliant mechanisms by assuming the flexure hinge as a joint with the spring [18, 19]. Ma [20], Xu [21], Mottard [22] and Qi [23] proposed kinematic and static models for rhombus /bridge-type amplifiers based on the elastic beam theory. The accuracy of these models was recently enhanced by Ling et al [9]. Meanwhile, the elastic beam theory was also employed to study the displacement attenuation in multistage compliant mechanisms [24]. Lobontiu and other scholars employed the Castigliano's second theorem to analyze the static performance of typical compliant mechanisms [8, 12, 25]. Generally, the elastic beam theory and the Castigliano's second theorem are popular for simple configurations. For complex compliant mechanisms or their composed systems with all kinds of flexure hinges, kinematic/static modeling can resort to the compliance matrix method. Li and other scholars carried out plenty of static modeling for precision positioning stages using the compliance matrix method [13, 26, 27]. Pham et al [28] and recently Lobontiu [29], Jiang et al [30] separately proposed static modeling method for complex compliant mechanisms with serial-parallel substructures based on the compliance matrix method. However, the modeling procedures are still complicated. A modeling method similar to the rigid multi-body dynamics proposed by Ryu et al [31] has been further developed and is now used for static/dynamic analyses of precision positioning stages [32, 33]. It should also be noted that only the compliance of the flexure hinge was considered while that of the flexible beam was neglected in almost all of the aforementioned modeling methods, which may lead to low prediction accuracy.

The contribution of this paper is to present a general and accurate kinematic/static modeling method for flexure-hinge-based compliant mechanisms with complex serial-parallel substructures and distributed/hybrid compliance by flexibly combining the displacement matrix method with the transfer matrix method. The paper is limited to planar mechanisms due to their extensive applications. It can be extended to spatial cases with a similar procedure. Besides, this paper mainly deals with the problem of small deformations. For nonlinearly large deformation, the readers are recommended to refer to the previous works of Howell [1], Awta [34], Chen [17] or others. Interestingly, these previous pseudo-rigid-body or nonlinear models can be further modified and included as an element or a module into the presented general model for large deformations.

The paper is organized as follows. A general kinematic/static modeling approach without condensation is presented in Section 2. The condensed modeling procedure is conducted in Section 3. The consideration of the rotational motion for multi-DOF compliant mechanisms is discussed in Section 4. Then, summary of the proposed modeling methodology as well as its numerical/experimental verifications are illustrated in Section 5 and Section 6, respectively. The conclusions are made in the final section.

2. Kinematic/static modeling procedure

In applications, most flexure-hinge-based compliant mechanisms are organized serially and/or in parallel. Figure 1 (a) provides the configuration of a piezo-actuated precision positioning stage. It is formed by serial and parallel branch chains with three parts: (i) flexure hinge; (ii) flexible beam (the guiding beams are termed as 'flexible beam'); and (iii) lumped mass (e.g. output port). It can represent many cases in applications. Figure 1 (b) is a general topology abstracted from Figure 1 (a), which will be used as the exemplary configuration for the proposed modeling procedure.

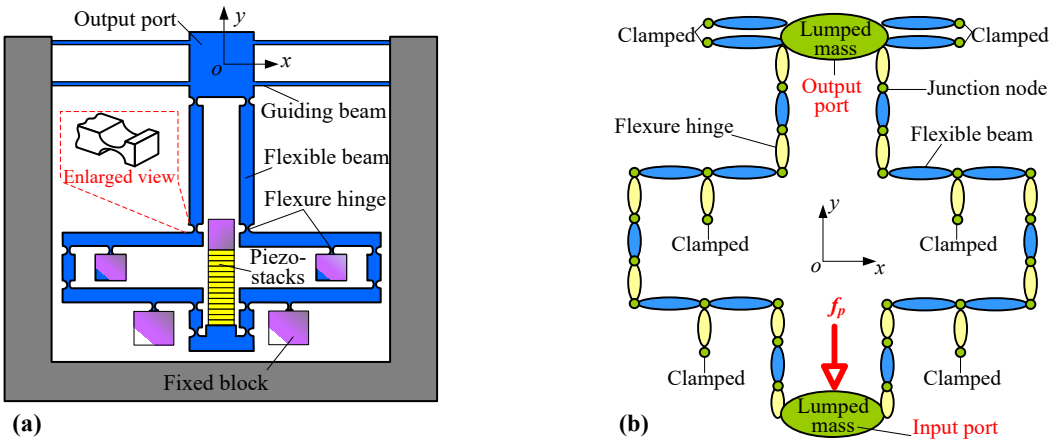

Figure 1 A compliant mechanism with serial-parallel sub-chains and its topology. (a) Exemplary configuration. (b) General topology with flexure hinges shown in yellow and flexible beam in blue.

Figure 2 illustrates the serial and parallel branch chains cut from the topology in Figure 1 (b). A serial branch chain is composed of several flexible beams interconnected by flexure hinges with the characteristics of one junction node connecting only two elements, while one junction node has at least three elements interconnected in a parallel branch chain.

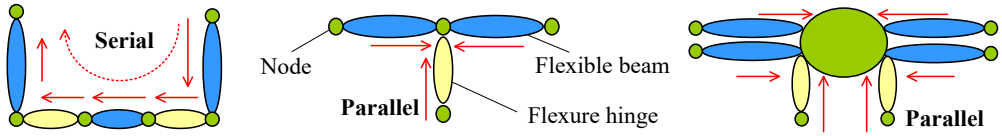

Figure 2 Illustration of serial and parallel substructures.

The proposed modeling procedure consists of three steps:

Step 1: Discretization and numbering

The compliant mechanism in Figure 1 is discretized into the flexure hinge, the flexible beam and the lumped mass according to the configuration and the degree of deformation. The flexure hinge bears the largest deformation and the flexible beam bears different levels of deformation in different configurations. As shown in Figure 1 (a), the guiding beams bear large deformation while the flexible beams bear small deformation. In the proposed modeling method, the compliance of the flexure hinge and the flexible beam are both considered. The lumped mass bears little deformation compared to other elements. As shown in Figure 3, the flexure hinges and the flexible beams are denoted serially from (1) to (34) and are connected with nodes from 1 to 34. The actuating force is denoted as f_p. It should be noted that the contact beam with the piezo-stacks is modeled as a rigid lumped mass, which is constant with practice where contact beam is often designed to be thick without deformation to enhance the

output displacement of compliant mechanisms. After discretizing, the compliant mechanism is transformed into a topology possessing a finite number of degrees of freedom.

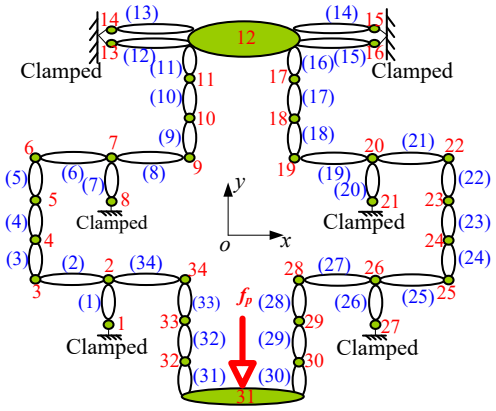

Figure 3 Discretization and numbering of the mechanism.

Step 2: Elemental stiffness matrix

As shown in Figure 4, each flexible beam is a uniform cross-section beam while the flexure hinge is regarded as a variable cross-section beam. Both of the resulting beam-like elements have two nodes, j and k, with three degrees of freedom per node: axial displacements u_j and u_k; transverse deflections w_j and w_k and rotations θ_j and θ_k in the local coordinate system $o_ix_iy_i$. The nodal displacement of the ith beam-like element in the local frame can be expressed as

$$\{\overline{\boldsymbol{q}}_i\} = \left[u_j, w_j, \theta_j, u_k, w_k, \theta_k\right]^{\mathrm{T}} \tag{1}$$

where subscripts j and k denote the serial number of nodes connected to the ith beam-like element. Superscript T denotes the transpose of a matrix.

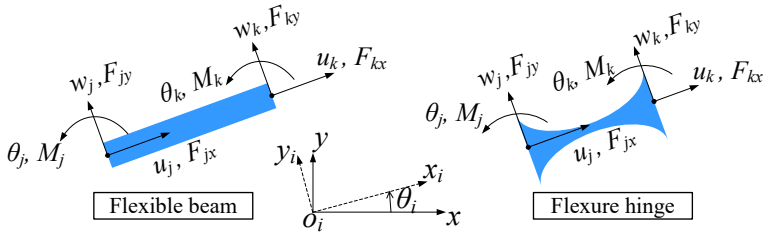

Figure 4 Nodal displacement and nodal force of the *i*th beam-like element.

The nodal force of the ith beam-like element, $\{\overline{\boldsymbol{F}}_i\} = \left[F_{jx}, F_{jy}, M_j, F_{kx}, F_{ky}, M_k\right]^{\mathrm{T}}$, in the local coordinate system can be expressed in the form of generalized Hooke's law

$$\{\overline{\boldsymbol{F}}_i\} = \overline{\boldsymbol{K}}_i \cdot \{\overline{\boldsymbol{q}}_i\} \tag{2}$$

where $\overline{\boldsymbol{K}}_i$ is the elemental stiffness matrix of the ith beam-like element.

For the flexible beam with uniform cross-section, its elemental stiffness matrix, $\overline{\boldsymbol{K}}_i$, in the local coordinate system can be found from finite element theory as

$$\overline{\boldsymbol{K}}_i^b = \begin{bmatrix} EA_i/l_i & 0 & 0 & -EA_i/l_i & 0 & 0 \\ & 12EI_i/(1+\beta)l_i^3 & 6EI_i/(1+\beta)l_i^2 & 0 & -12EI_i/(1+\beta)l_i^3 & 6EI_i/(1+\beta)l_i^2 \\ & & (4+\beta)EI_i/(1+\beta)l_i & 0 & -6EI_i/(1+\beta)l_i^2 & (2-\beta)EI_i/(1+\beta)l_i \\ & & & EA_i/l_i & 0 & 0 \\ & Sym & & & 12EI_i/(1+\beta)l_i^3 & -6EI_i/(1+\beta)l_i^2 \\ & & & & & (4+\beta)EI_i/(1+\beta)l_i \end{bmatrix} \tag{3}$$

where superscript b denotes the flexible beam. A_i and I_i are the area and moment of inertia about the neutral axis of the cross-section. E is the Young's modulus. l_i is the length of the ith beam-like element. Here, a Timoshenko beam is considered and $\beta=12EI_i/\kappa GA_i l_i^2$, where G is the shear modulus, $\kappa=5/6$; $\beta=0$ means an Euler-Bernoulli beam.

For the flexure hinge, its cross section is variable. Its elemental stiffness matrix in Eq. (2) can not be easily and accurately calculated. Actually, analytical formulas [35, 36] and empirical models [37, 38] for the compliance matrix of flexure hinges featuring elliptical, corner-filleted, circular, and so on, were developed in the past investigations. Therefore, the elemental stiffness matrix of the flexure hinge needed here can be transformed from the existing analytical compliance matrix of generic flexure hinges.

Assuming a planar flexure hinge as a 3-DOF elastic element, its compliance matrix, $\boldsymbol{C}_i$, can be expressed as a standard form in its local coordinate system $o_i x_i y_i$ [35-38] as

$$\boldsymbol{C}_i = \begin{bmatrix} c_x & 0 & 0 \\ 0 & c_y & c_\alpha \\ 0 & c_\alpha & c_\theta \end{bmatrix} = \begin{bmatrix} k_x & 0 & 0 \\ 0 & k_y & k_\alpha \\ 0 & k_\alpha & k_\theta \end{bmatrix}^{-1} \tag{4}$$

where c_x c_y, c_α, c_θ and k_x k_y, k_α, k_θ are the coefficients of the compliance matrix $\boldsymbol{C}_i$ and its inverse. The detailed expressions can be found from previous papers [35-38].

The elemental stiffness matrix of the ith flexure hinge, $\bar{\boldsymbol{K}}_i$, can be deduced as the function of the coefficients in Eq. (4). The detailed derivation is listed in Appendix A, and the ultimate expression is shown in Eq. (5).

$$\bar{\boldsymbol{K}}_i^h = \begin{bmatrix} k_x & 0 & 0 & -k_x & 0 & 0 \\ & k_y & -k_\alpha & 0 & -k_y & -k_\alpha \\ & & k_\theta & 0 & k_\alpha & -l_i \cdot k_\alpha - k_\theta \\ & & & k_x & 0 & 0 \\ & Sym & & & k_y & k_\alpha \\ & & & & & k_\theta \end{bmatrix} \tag{5}$$

Eq. (5) bridges the theoretical compliance matrix in previous literature with the elemental stiffness matrix needed here. It should be noted that since the ratio of length to thickness of the flexure hinge is small, shear deformation should be considered when choosing a compliance matrix for calculating Eq. (5).

By performing rotation transformation, the nodal displacement and the nodal force in the local frame $o_i x_i y_i$ can be expressed in the reference frame $oxyz$, so Eq. (2) is expressed as

$$\{\boldsymbol{F}_i\} = \boldsymbol{K}_i \cdot \{\boldsymbol{q}_i\} \tag{6}$$

where $\{\boldsymbol{F}_i\} = \boldsymbol{R}_i^{\mathrm{T}} \{\bar{\boldsymbol{F}}_i\}$, $\{\boldsymbol{q}_i\} = \boldsymbol{R}_i^{\mathrm{T}} \{\bar{\boldsymbol{q}}_i\}$, $\boldsymbol{K}_i = \boldsymbol{R}_i^{\mathrm{T}} \bar{\boldsymbol{K}}_i \boldsymbol{R}_i$. Rotation matrix $\boldsymbol{R}_i$ is determined by the orientation of the ith beam-like element. As illustrated in Figure 4, θ_i is the rotational angle of the ith local frame with respect to the reference frame, and $\boldsymbol{R}_i$ can be written as

$$\boldsymbol{R}_i = \begin{bmatrix} \cos\theta_i & \sin\theta_i & 0 & 0 & 0 & 0 \\ -\sin\theta_i & \cos\theta_i & 0 & 0 & 0 & 0 \\ 0 & 0 & 1 & 0 & 0 & 0 \\ 0 & 0 & 0 & \cos\theta_i & \sin\theta_i & 0 \\ 0 & 0 & 0 & -\sin\theta_i & \cos\theta_i & 0 \\ 0 & 0 & 0 & 0 & 0 & 1 \end{bmatrix} \tag{7}$$

Step 3: Static modeling without condensation

Eq. (6), which describes the elastic relations between the nodal force and the nodal displacement of the ith beam-like element, can be rewritten as

$$\begin{Bmatrix} \boldsymbol{F}_{ij} \\ \boldsymbol{F}_{ik} \end{Bmatrix} = \begin{bmatrix} \boldsymbol{k}_{i,1} & \boldsymbol{k}_{i,2} \\ \boldsymbol{k}_{i,3} & \boldsymbol{k}_{i,4} \end{bmatrix} \cdot \begin{Bmatrix} \boldsymbol{x}_j \\ \boldsymbol{x}_k \end{Bmatrix} \tag{8}$$

where $\boldsymbol{F}_{ij}$ and $\boldsymbol{F}_{ik}$ are, respectively, the nodal force vector of the j-end and the k-end in the ith beam-like element. $\{\boldsymbol{x}_j\}=[u_j, w_j, \theta_j]^{\mathrm{T}}$ and $\{\boldsymbol{x}_k\}=[u_k, w_k, \theta_k]^{\mathrm{T}}$ are the two nodal displacements of the ith beam-like element in the reference frame, as shown in Figure 4.

Taking each node as the study object, the force exerted on the node by its connected elements is the sum of the inverse nodal force of the corresponding beam-like elements. Thus, the following force balance equation can be obtained for the nth node

$$\sum\nolimits_N \boldsymbol{F}_{ij(k)} = \boldsymbol{P}_n \tag{9}$$

where N is the total number of elements connected to the nth node. $\boldsymbol{F}_{ij(k)}$ is the nodal force of the j end or k end of the ith beam-like element. Because the nth node may be connected to the j end or k end of the ith beam-like element as shown in Figure 3, so $\boldsymbol{F}_{ij(k)}$ is set to $\boldsymbol{F}_{ij}$ if the nth node is connected to j end; otherwise $\boldsymbol{F}_{ij(k)}$ is set to $\boldsymbol{F}_{ik}$. $\boldsymbol{P}_n$ is the sum of external force directly exerted on the nth node and the equivalent force from intra-elemental force. For the mechanism in Figure 3, only a lumped piezo-actuated force f_p acts on the node of 31 and no force acts on the intra-elements, so $\boldsymbol{P}_{31}=[0, -f_p, 0]^{\mathrm{T}}$ and $\boldsymbol{P}_n=\boldsymbol{0}$ for other nodes.

By substituting Eq. (8) into Eq. (9), the following equation can be obtained

$$\sum\nolimits_N \left((\boldsymbol{k}_{i,1}\boldsymbol{x}_j + \boldsymbol{k}_{i,2}\boldsymbol{x}_k) \ \ or \ \ (\boldsymbol{k}_{i,3}\boldsymbol{x}_j + \boldsymbol{k}_{i,4}\boldsymbol{x}_k) \right) = \boldsymbol{P}_n \tag{10}$$

where the former is selected if the nth node is connected to the j end of the ith beam-like element; the latter is valid when the elemental force exerted on the node is from the k end.

Eq. (10) is the force equilibrium equation of the nth node. Considering the force balance of all nodes in sequence, and noting that the nodal displacements of clamped nodes 1, 8, 13, 14, 15, 16, 21 and 27 in Figure 3 are zero, i.e. $\boldsymbol{x}_1=\boldsymbol{x}_8=\boldsymbol{x}_{13}=\boldsymbol{x}_{14}=\boldsymbol{x}_{15}=\boldsymbol{x}_{16}=\boldsymbol{x}_{21}=\boldsymbol{x}_{27}=\boldsymbol{0}$, then the static model of the whole compliant mechanism taking the nodal displacement vector as the variables can be established. The equilibrium equations of selected nodes 2, 3 and 31 are given to illustrate the static model. The balance equations for other nodes can be easily obtained based on Eq. (10) but are not listed here

$$\begin{cases} \text{node 2:} \quad (\boldsymbol{k}_{1,4} + \boldsymbol{k}_{2,1} + \boldsymbol{k}_{34,4})\boldsymbol{x}_2 + \boldsymbol{k}_{2,2}\boldsymbol{x}_3 + \boldsymbol{k}_{34,3}\boldsymbol{x}_{34} = \boldsymbol{0} \\ \text{node 3:} \quad \boldsymbol{k}_{2,3}\boldsymbol{x}_2 + (\boldsymbol{k}_{2,4} + \boldsymbol{k}_{3,1})\boldsymbol{x}_3 + \boldsymbol{k}_{3,2}\boldsymbol{x}_4 = \boldsymbol{0} \\ \text{node 31:} \ \boldsymbol{k}_{30,3}\boldsymbol{x}_{30} + (\boldsymbol{k}_{30,4} + \boldsymbol{k}_{31,1})\boldsymbol{x}_{31} + \boldsymbol{k}_{31,2}\boldsymbol{x}_{32} = \boldsymbol{F}_p \end{cases} \tag{11}$$

where $\boldsymbol{k}_{i,1}$, $\boldsymbol{k}_{i,2}$, $\boldsymbol{k}_{i,3}$, $\boldsymbol{k}_{i,4}$ are the coefficients of the elemental block stiffness matrix in Eq. (8).

The force equilibrium equations of all nodes constitute a linear equation set, which is the static model of the whole compliant mechanism and contains twenty-six vector equations for the compliant mechanism in Figure 3. The set can be solved, and the kinematic and static performance such as the displacement amplification ratio and the input/output stiffness can be then obtained. The y-component of $\boldsymbol{x}_{31}$ and $\boldsymbol{x}_{12}$ are respectively the input and the output displacement of the mechanism in Figure 3, Therefore, when actuating force f_p is applied, the displacement amplification ratio R and the input stiffness K_{in} of the compliant mechanism can be calculated as

$$R = \frac{\boldsymbol{x}_{12(y)}}{\boldsymbol{x}_{31(y)}}, \quad K_{in} = \frac{f_p}{\boldsymbol{x}_{31(y)}} \tag{12}$$

where $\boldsymbol{x}_{12(y)}$ and $\boldsymbol{x}_{31(y)}$ are respectively the displacement of node 12 and node 31 in the y axis.

3. Kinematic/static modeling with condensed configuration

The static model presented in Section 2 requires solving an equilibrium equation set with large degrees of freedom. In this section, the transfer matrix method is flexibly combined with the above matrix displacement method to condense a serial-parallel branch chain into an equivalent element to further establish the input/output force-displacement relations of a compliant mechanism. As shown in Figure 5, by condensing twice, the local parallel and serial substructures are simplified as two elements with equivalent stiffness matrix.

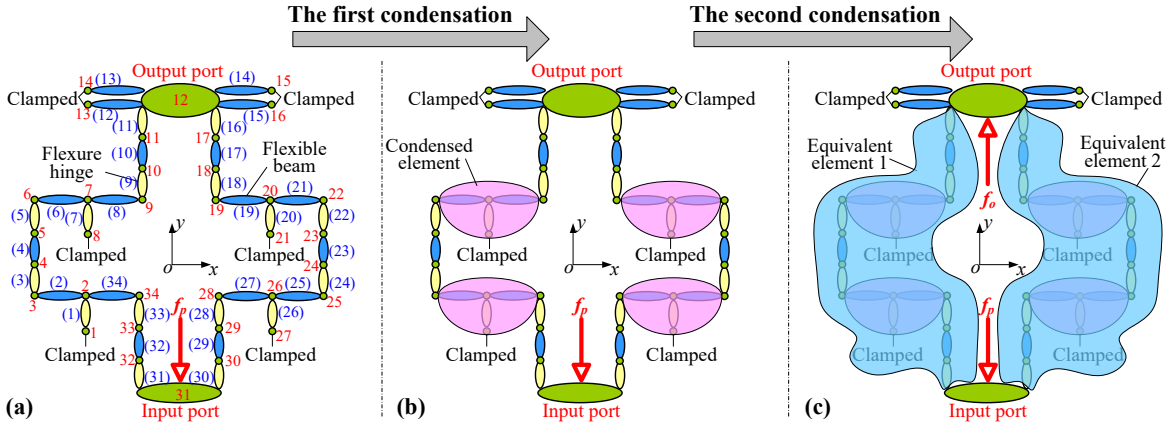

Figure 5 Condensed configuration by the transfer matrix method

As shown in Figure 5 (b), the locally parallel chain with three elements interconnected at one common node is first condensed as one equivalent beam-like element. The equivalent elemental stiffness matrix is deduced for node 2 in the following and a similar model can be built for the other three parallel sub-chains. Taking node 2 as the study object, forces on this node exerted by its connected elements are the sum of the inverse nodal forces of these connected elements

$$\boldsymbol{F}_{1k} + \boldsymbol{F}_{2j} + \boldsymbol{F}_{34k} = \boldsymbol{0} \tag{13}$$

By substituting the nodal force with the nodal displacement in Eq. (8), the force balance equation of node 2, i.e. Eq. (13), is transferred to

$$\boldsymbol{k}_{1,3}\boldsymbol{x}_1 + (\boldsymbol{k}_{1,4} + \boldsymbol{k}_{2,1} + \boldsymbol{k}_{34,4})\boldsymbol{x}_2 + \boldsymbol{k}_{2,2}\boldsymbol{x}_3 + \boldsymbol{k}_{34,3}\boldsymbol{x}_{34} = \boldsymbol{0} \tag{14}$$

The nodal force of element (2) at the k end, i.e. at the end of node 3, and the nodal force of element (34) at the j end, i.e. at the end of node 34, can be written based on Eq. (8) as

$$\begin{cases} \boldsymbol{F}_{2k} = \boldsymbol{k}_{2,3}\boldsymbol{x}_2 + \boldsymbol{k}_{2,4}\boldsymbol{x}_3 \\ \boldsymbol{F}_{34j} = \boldsymbol{k}_{34,1}\boldsymbol{x}_{34} + \boldsymbol{k}_{34,2}\boldsymbol{x}_2 \end{cases} \tag{15}$$

Substituting Eq. (14) into Eq. (15) and eliminating intermediate variable $\boldsymbol{x}_2$, also noting that the nodal displacement of clamped node 1 is zero, i.e. $\boldsymbol{x}_1=\boldsymbol{0}$, the equivalent elemental stiffness matrix of the condensed element can be solved as

$$\begin{Bmatrix} \boldsymbol{F}_{34j} \\ \boldsymbol{F}_{2k} \end{Bmatrix} = \begin{bmatrix} \boldsymbol{k}_{34,1} - \boldsymbol{k}_{34,2}\cdot(\boldsymbol{k}_{1,4} + \boldsymbol{k}_{2,1} + \boldsymbol{k}_{34,4})^{-1}\cdot\boldsymbol{k}_{34,3} & -\boldsymbol{k}_{34,2}\cdot(\boldsymbol{k}_{1,4} + \boldsymbol{k}_{2,1} + \boldsymbol{k}_{34,4})^{-1}\cdot\boldsymbol{k}_{2,2} \\ -\boldsymbol{k}_{2,3}\cdot(\boldsymbol{k}_{1,4} + \boldsymbol{k}_{2,1} + \boldsymbol{k}_{34,4})^{-1}\cdot\boldsymbol{k}_{34,3} & \boldsymbol{k}_{2,4} - \boldsymbol{k}_{2,3}\cdot(\boldsymbol{k}_{1,4} + \boldsymbol{k}_{2,1} + \boldsymbol{k}_{34,4})^{-1}\cdot\boldsymbol{k}_{2,2} \end{bmatrix} \cdot \begin{Bmatrix} \boldsymbol{x}_{34} \\ \boldsymbol{x}_3 \end{Bmatrix} \tag{16}$$

Through the first condensation, the hybrid serial-parallel chain becomes a sole serial chain, and the resulting serial chain can be further condensed as one equivalent element with the transfer matrix method, as shown in Figure 5 (c). The transfer matrix of the ith beam-like element or the equivalent element in the reference frame can be easily deduced from Eq. (8) as

$$\begin{Bmatrix} \boldsymbol{x}_k \\ -\boldsymbol{F}_{ik} \end{Bmatrix} = \boldsymbol{T}_i \cdot \begin{Bmatrix} \boldsymbol{x}_j \\ \boldsymbol{F}_{ij} \end{Bmatrix} = \begin{bmatrix} \boldsymbol{t}_{i,1} & \boldsymbol{t}_{i,2} \\ \boldsymbol{t}_{i,3} & \boldsymbol{t}_{i,4} \end{bmatrix} \cdot \begin{Bmatrix} \boldsymbol{x}_j \\ \boldsymbol{F}_{ij} \end{Bmatrix} = \begin{bmatrix} -\boldsymbol{k}_{i,2}^{-1} \cdot \boldsymbol{k}_{i,1} & \boldsymbol{k}_{i,2}^{-1} \\ -\boldsymbol{k}_{i,3} + \boldsymbol{k}_{i,4} \cdot \boldsymbol{k}_{i,2}^{-1} \cdot \boldsymbol{k}_{i,1} & -\boldsymbol{k}_{i,4} \cdot \boldsymbol{k}_{i,2}^{-1} \end{bmatrix} \cdot \begin{Bmatrix} \boldsymbol{x}_j \\ \boldsymbol{F}_{ij} \end{Bmatrix} \tag{17}$$

where the global transfer matrix $\boldsymbol{T}_i$ of the ith beam-like element or the equivalent element relates the displacements and forces at both ends of the element.

Through the condensation in Figure 5 (c), the transfer matrices of the new equivalent elements transferred from the serial chains in Figure 5 (b), are

$$\begin{cases} \boldsymbol{T}_1^{(II)} = \boldsymbol{T}_{11} \cdot \boldsymbol{T}_{10} \cdot \boldsymbol{T}_9 \cdot \boldsymbol{T}_2^{(I)} \cdot \boldsymbol{T}_5 \cdot \boldsymbol{T}_4 \cdot \boldsymbol{T}_3 \cdot \boldsymbol{T}_1^{(I)} \cdot \boldsymbol{T}_{33} \cdot \boldsymbol{T}_{32} \cdot \boldsymbol{T}_{31} \\ \boldsymbol{T}_2^{(II)} = \boldsymbol{T}_{16} \cdot \boldsymbol{T}_{17} \cdot \boldsymbol{T}_{18} \cdot \boldsymbol{T}_3^{(I)} \cdot \boldsymbol{T}_{22} \cdot \boldsymbol{T}_{23} \cdot \boldsymbol{T}_{24} \cdot \boldsymbol{T}_4^{(I)} \cdot \boldsymbol{T}_{28} \cdot \boldsymbol{T}_{29} \cdot \boldsymbol{T}_{30} \end{cases} \tag{18}$$

where superscript (II) denotes the second condensation. $\boldsymbol{T}_i^{(I)}$ (i=1,2,3,4) are the four transfer matrices of the equivalent element in Figure 5 (b).

Then, the equivalent elemental stiffness matrix of the new condensed element in Figure 5 (c) can be again obtained from the corresponding transfer matrix $\boldsymbol{T}_1^{(II)}$ and $\boldsymbol{T}_2^{(II)}$ in Eq. (18)

$$\begin{Bmatrix} \boldsymbol{F}_{ij} \\ \boldsymbol{F}_{ik} \end{Bmatrix} = \boldsymbol{K}_i^{(II)} \cdot \begin{Bmatrix} \boldsymbol{x}_j \\ \boldsymbol{x}_k \end{Bmatrix} = \begin{bmatrix} \boldsymbol{k}_{i,1}^{(II)} & \boldsymbol{k}_{i,2}^{(II)} \\ \boldsymbol{k}_{i,3}^{(II)} & \boldsymbol{k}_{i,4}^{(II)} \end{bmatrix} \cdot \begin{Bmatrix} \boldsymbol{x}_j \\ \boldsymbol{x}_k \end{Bmatrix} = \begin{bmatrix} -\boldsymbol{t}_{i,2}^{-1} \cdot \boldsymbol{t}_{i,1} & \boldsymbol{t}_{i,2}^{-1} \\ -\boldsymbol{t}_{i,3} + \boldsymbol{t}_{i,4} \cdot \boldsymbol{t}_{i,2}^{-1} \cdot \boldsymbol{t}_{i,1} & -\boldsymbol{t}_{i,4} \cdot \boldsymbol{t}_{i,2}^{-1} \end{bmatrix} \cdot \begin{Bmatrix} \boldsymbol{x}_j \\ \boldsymbol{x}_k \end{Bmatrix} \tag{19}$$

As shown in Figure 5 (c), after performing condensation twice, the compliant mechanism is configured into a two-port mechanical network model. Considering node 12 at the output port and node 31 at the input port, and noting that the nodal displacements of clamped nodes 13, 14, 15, 16 are all zero, i.e. $\boldsymbol{x}_{13}$=$\boldsymbol{x}_{14}$=$\boldsymbol{x}_{15}$=$\boldsymbol{x}_{16}$=$\boldsymbol{0}$, the equilibrium equation of the nodal force can be respectively established as

$$\begin{cases} (\boldsymbol{k}_{1,1}^{(II)} + \boldsymbol{k}_{2,1}^{(II)}) \cdot \boldsymbol{x}_{31} + (\boldsymbol{k}_{1,2}^{(II)} + \boldsymbol{k}_{2,2}^{(II)}) \cdot \boldsymbol{x}_{12} = \boldsymbol{F}_p \\ (\boldsymbol{k}_{1,3}^{(II)} + \boldsymbol{k}_{2,3}^{(II)}) \cdot \boldsymbol{x}_{31} + (\boldsymbol{k}_{1,4}^{(II)} + \boldsymbol{k}_{2,4}^{(II)} + \boldsymbol{k}_{12,1} + \boldsymbol{k}_{13,1} + \boldsymbol{k}_{14,1} + \boldsymbol{k}_{15,1}) \cdot \boldsymbol{x}_{12} = \boldsymbol{F}_o \end{cases} \tag{20}$$

where $\boldsymbol{F}_o$ is a virtual force acting on the output port to further calculate the output stiffness.

Eq. (20) can be further rewritten as a more general form by defining input, output and coupled stiffness. Thus, the input/output force-displacement relations of the equivalent two-port mechanical network of the compliant mechanism have the standard form of the generalized Hooke's law as

$$\begin{pmatrix} \boldsymbol{F}_p \\ \boldsymbol{F}_o \end{pmatrix} = \begin{bmatrix} \boldsymbol{K}_{in} & \boldsymbol{K}_{co} \\ \boldsymbol{K}_{co} & \boldsymbol{K}_{out} \end{bmatrix} \cdot \begin{pmatrix} \boldsymbol{x}_{in} \\ \boldsymbol{x}_{out} \end{pmatrix} \text{ with}$$

$$\begin{bmatrix} \boldsymbol{K}_{in} & \boldsymbol{K}_{co} \\ \boldsymbol{K}_{co} & \boldsymbol{K}_{out} \end{bmatrix} = \begin{bmatrix} \boldsymbol{k}_{1,1}^{(II)} + \boldsymbol{k}_{2,1}^{(II)} & \boldsymbol{k}_{1,2}^{(II)} + \boldsymbol{k}_{2,2}^{(II)} \\ \boldsymbol{k}_{1,3}^{(II)} + \boldsymbol{k}_{2,3}^{(II)} & \boldsymbol{k}_{1,4}^{(II)} + \boldsymbol{k}_{2,4}^{(II)} + \boldsymbol{k}_{12,1} + \boldsymbol{k}_{13,1} + \boldsymbol{k}_{14,1} + \boldsymbol{k}_{15,1} \end{bmatrix} \tag{21}$$

where $\boldsymbol{k}_{in}$, $\boldsymbol{k}_{out}$ and $\boldsymbol{k}_{co}$ are the elements of the equivalent stiffness matrix of the two-port mechanical network of the compliant mechanism.

In this way, the internal DOFs of each serial and parallel substructure do not appear in the static model but only the input/output force-displacement relations. Based on Eq. (21), the displacement amplification ratio and the input stiffness of the compliant mechanism can be easily obtained by letting $\boldsymbol{F}_o$=0, which has the same results as Eq. (12). The significance of the two-port mechanical network model, i.e. Eq. (21), is that it comprehensively describes the kinematic and static characteristics of the compliant mechanism from the viewpoint of input and output ports without the need to care about the internal DOFs. With the two-port mechanical network model, the kinematic and static performances of a compliant mechanism can be calculated.

4. Consideration of rotational lumped mass

The lumped mass in the preceding sections was simplified as a node without considering

the rotary DOF, which is exactly accurate for compliant mechanisms with only translational motions, such as X, Y and XY flexible manipulators. However, the dimensions and the rotary DOF of the lumped mass should be included for compliant mechanisms with rotary motion. Figure 6 shows an XYθ compliant mechanism. The representative configuration was widely investigated in previous applications [31, 39] and is adopted here as an example to illustrate the modeling procedure for rotary lumped mass.

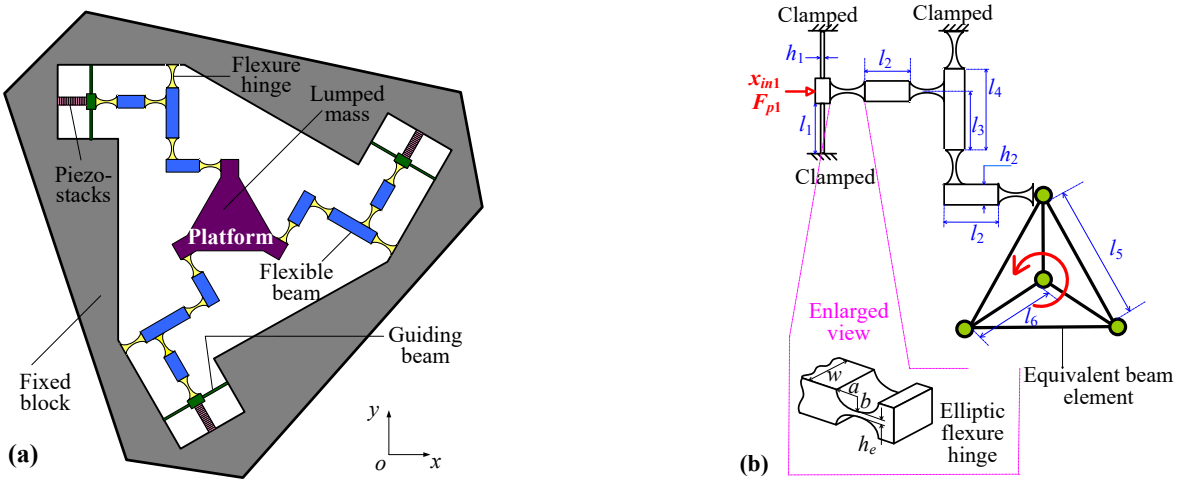

Figure 6 Exemplary mechanism with rotational DOF. (a) Exemplary configuration. (b) Local structure and geometric parameters. (Noting: the configuration is not an optimal stage and is used to illustrate the modeling procedure)

As shown in Figure 6 (b), the triangular platform with lumped mass can be equivalent to six beam-like elements with four nodes. Each node has one rotational and two translational degrees of freedom, and the displacement vector of the central node is defined as the output displacement of the compliant mechanism. As shown in Figure 7 (a), only one limb and the platform are needed to number considering the symmetry of the configuration. Elements (1) ~ (3) constitute a local parallel chain interconnected at node 1. Considering node 1, forces exerted on the node by its connected elements is the sum of the inverse nodal forces of the corresponding elements. And by substituting the nodal force with the nodal displacement in Eq. (8), also noting that the nodal displacements of clamped node 2 and node 3 are zero, the force balance equation of node 1 is

$$\boldsymbol{F}_{p1} = (\boldsymbol{k}_{1,1} + \boldsymbol{k}_{2,1} + \boldsymbol{k}_{3,1})\boldsymbol{x}_{in1} + \boldsymbol{k}_{3,2}\boldsymbol{x}_4 \tag{22}$$

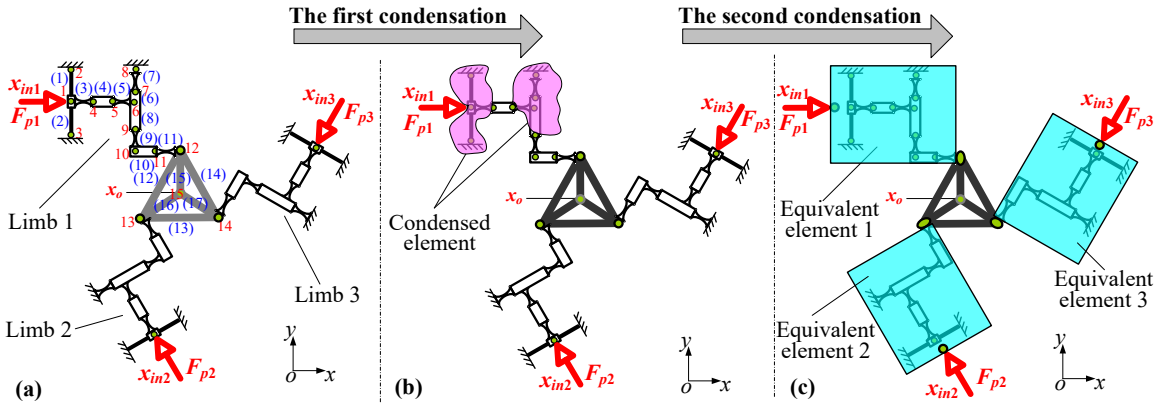

Figure 7 Condensed configuration by the transfer matrix method

The nodal force of element (3) at the end of node 4 can be written based on Eq. (8) as

$$\boldsymbol{F}_{3k} = \boldsymbol{k}_{3,3}\boldsymbol{x}_{in1} + \boldsymbol{k}_{3,4}\boldsymbol{x}_4 \tag{23}$$

By combining Eq. (22) and Eq. (23), the equivalent elemental stiffness matrix of the new condensed element is

$$\begin{Bmatrix} \boldsymbol{F}_{p1} \\ \boldsymbol{F}_{3k} \end{Bmatrix} = \boldsymbol{K}_1^{(I)} \cdot \begin{Bmatrix} \boldsymbol{x}_{in1} \\ \boldsymbol{x}_4 \end{Bmatrix} = \begin{bmatrix} \boldsymbol{k}_{1,1} + \boldsymbol{k}_{2,1} + \boldsymbol{k}_{3,1} & \boldsymbol{k}_{3,2} \\ \boldsymbol{k}_{3,3} & \boldsymbol{k}_{3,4} \end{bmatrix} \cdot \begin{Bmatrix} \boldsymbol{x}_{in1} \\ \boldsymbol{x}_4 \end{Bmatrix} \tag{24}$$

Similarly, Elements (5), (6), (7) and (8) constitute a local parallel chain interconnected at node 6. By using the similar procedure as Eq. (24), the equivalent elemental stiffness matrix of the new condensed element can also be deduced as

$$\begin{Bmatrix} \boldsymbol{F}_{5j} \\ \boldsymbol{F}_{9k} \end{Bmatrix} = \boldsymbol{K}_2^{(I)} \cdot \begin{Bmatrix} \boldsymbol{x}_5 \\ \boldsymbol{x}_9 \end{Bmatrix} = \begin{bmatrix} \boldsymbol{k}_{5,1} - \boldsymbol{k}_{5,2}(\boldsymbol{k}_x)^{-1}\boldsymbol{k}_{5,3} & -\boldsymbol{k}_{5,2}(\boldsymbol{k}_x)^{-1}\boldsymbol{k}_{8,2} \\ -\boldsymbol{k}_{8,3}(\boldsymbol{k}_x)^{-1}\boldsymbol{k}_{5,3} & \boldsymbol{k}_{8,4} - \boldsymbol{k}_{8,3}(\boldsymbol{k}_x)^{-1}\boldsymbol{k}_{8,2} \end{bmatrix} \cdot \begin{Bmatrix} \boldsymbol{x}_5 \\ \boldsymbol{x}_9 \end{Bmatrix} \tag{25}$$

where intermediate variable $\boldsymbol{k}_x = \boldsymbol{k}_{5,4} + \boldsymbol{k}_{8,1} + \boldsymbol{k}_{6,1} - \boldsymbol{k}_{6,2}(\boldsymbol{k}_{6,4} + \boldsymbol{k}_{7,1})^{-1}\boldsymbol{k}_{6,3}$.

As shown in Figure 7 (b), through the first condensation, the serial-parallel chain in limb 1 becomes a sole serial chain. The resulting serial chain is again condensed into one equivalent element with the transfer matrix method, as shown in Figure 7 (c). The transfer matrix of the new equivalent element in Figure 7 (c) can be calculated as

$$\boldsymbol{T}_{in1} = \boldsymbol{T}_{11} \cdot \boldsymbol{T}_{10} \cdot \boldsymbol{T}_9 \cdot \boldsymbol{T}_2^{(I)} \cdot \boldsymbol{T}_4 \cdot \boldsymbol{T}_1^{(I)} \tag{26}$$

where the global transfer matrix $\boldsymbol{T}_1^{(I)}$ and $\boldsymbol{T}_2^{(I)}$ are, respectively, the transfer matrix of the equivalent stiffness matrix of $\boldsymbol{K}_1^{(I)}$ and $\boldsymbol{K}_2^{(I)}$ in Eq. (24) and Eq. (25).

Then, the equivalent elemental stiffness matrix $\boldsymbol{K}_{in1}$ of the new condensed element of limb 1 in Figure 7 (c) can be again obtained from the corresponding transfer matrix $\boldsymbol{T}_{in1}$ in Eq. (26). The transition formula is the same as Eq. (19) in Section 3 and is omitted here. Based on the equivalent stiffness matrix, the input/output force-displacement relations of the condensed element of limb 1 is

$$\begin{Bmatrix} \boldsymbol{F}_{in1} \\ \boldsymbol{F}_{out1} \end{Bmatrix} = \boldsymbol{K}_{in1} \cdot \begin{Bmatrix} \boldsymbol{x}_{in1} \\ \boldsymbol{x}_{12} \end{Bmatrix} = \begin{bmatrix} \boldsymbol{k}_{in1,1} & \boldsymbol{k}_{in1,2} \\ \boldsymbol{k}_{in1,3} & \boldsymbol{k}_{in1,4} \end{bmatrix} \cdot \begin{Bmatrix} \boldsymbol{x}_{in1} \\ \boldsymbol{x}_{12} \end{Bmatrix} \tag{27}$$

The equivalent stiffness matrices of other two limbs 2 and 3 can be obtained from $\boldsymbol{K}_{in1}$ by rotation transformation based on the symmetry of the compliant mechanism as

$$\begin{cases} \boldsymbol{K}_{in2} = \boldsymbol{R}_2^{\mathrm{T}} \cdot \boldsymbol{K}_{in1} \cdot \boldsymbol{R}_2 \\ \boldsymbol{K}_{in3} = \boldsymbol{R}_3^{\mathrm{T}} \cdot \boldsymbol{K}_{in1} \cdot \boldsymbol{R}_3 \end{cases} \tag{28}$$

where $\boldsymbol{R}_2$ and $\boldsymbol{R}_3$ are the rotation matrix in Eq. (7), the rotary angles in $\boldsymbol{R}_2$ and $\boldsymbol{R}_3$ are, respectively, -240 degree and -120 degree.

Then, the input/output force-displacement relations of the condensed element of these two limbs are, respectively

$$\begin{Bmatrix} \boldsymbol{F}_{in2} \\ \boldsymbol{F}_{out2} \end{Bmatrix} = (\boldsymbol{R}_2^{\mathrm{T}} \cdot \boldsymbol{K}_{in1} \cdot \boldsymbol{R}_2) \cdot \begin{Bmatrix} \boldsymbol{x}_{in2} \\ \boldsymbol{x}_{13} \end{Bmatrix} = \begin{bmatrix} \boldsymbol{k}_{in2,1} & \boldsymbol{k}_{in2,2} \\ \boldsymbol{k}_{in2,3} & \boldsymbol{k}_{in2,4} \end{bmatrix} \cdot \begin{Bmatrix} \boldsymbol{x}_{in2} \\ \boldsymbol{x}_{13} \end{Bmatrix} \tag{29}$$

$$\begin{Bmatrix} \boldsymbol{F}_{in3} \\ \boldsymbol{F}_{out3} \end{Bmatrix} = (\boldsymbol{R}_3^{\mathrm{T}} \cdot \boldsymbol{K}_{in1} \cdot \boldsymbol{R}_3) \cdot \begin{Bmatrix} \boldsymbol{x}_{in3} \\ \boldsymbol{x}_{14} \end{Bmatrix} = \begin{bmatrix} \boldsymbol{k}_{in3,1} & \boldsymbol{k}_{in3,2} \\ \boldsymbol{k}_{in3,3} & \boldsymbol{k}_{in3,4} \end{bmatrix} \cdot \begin{Bmatrix} \boldsymbol{x}_{in3} \\ \boldsymbol{x}_{14} \end{Bmatrix} \tag{30}$$

As shown in Figure 7 (c), considering the nodes 12, 13, 14 and 15, the equilibrium equations of the nodal force can be established as

$$\begin{cases} \text{node 12: } \boldsymbol{k}_{in1,3}\boldsymbol{x}_{in1} + (\boldsymbol{k}_{in1,4} + \boldsymbol{k}_{12,1} + \boldsymbol{k}_{14,1} + \boldsymbol{k}_{15,1})\boldsymbol{x}_{12} + \boldsymbol{k}_{12,2}\boldsymbol{x}_{13} + \boldsymbol{k}_{14,2}\boldsymbol{x}_{14} + \boldsymbol{k}_{15,2}\boldsymbol{x}_{out} = \boldsymbol{0} \\ \text{node 13: } \boldsymbol{k}_{in2,3}\boldsymbol{x}_{in2} + (\boldsymbol{k}_{in2,4} + \boldsymbol{k}_{12,4} + \boldsymbol{k}_{13,1} + \boldsymbol{k}_{16,1})\boldsymbol{x}_{13} + \boldsymbol{k}_{12,3}\boldsymbol{x}_{12} + \boldsymbol{k}_{13,2}\boldsymbol{x}_{14} + \boldsymbol{k}_{16,2}\boldsymbol{x}_{out} = \boldsymbol{0} \\ \text{node 14: } \boldsymbol{k}_{in3,3}\boldsymbol{x}_{in3} + (\boldsymbol{k}_{in3,4} + \boldsymbol{k}_{13,4} + \boldsymbol{k}_{14,4} + \boldsymbol{k}_{17,1})\boldsymbol{x}_{14} + \boldsymbol{k}_{14,3}\boldsymbol{x}_{12} + \boldsymbol{k}_{13,3}\boldsymbol{x}_{13} + \boldsymbol{k}_{17,2}\boldsymbol{x}_{out} = \boldsymbol{0} \\ \text{node 15: } \boldsymbol{k}_{15,3}\boldsymbol{x}_{12} + \boldsymbol{k}_{16,3}\boldsymbol{x}_{13} + \boldsymbol{k}_{17,3}\boldsymbol{x}_{14} + (\boldsymbol{k}_{15,4} + \boldsymbol{k}_{16,4} + \boldsymbol{k}_{17,4})\boldsymbol{x}_{out} = \boldsymbol{0} \end{cases} \tag{31}$$

Also, the following equations can be obtained from Eq. (27), Eq. (29) and Eq. (30) as

$$\begin{cases} \boldsymbol{F}_{in1} = \boldsymbol{k}_{in1,1}\boldsymbol{x}_{in1} + \boldsymbol{k}_{in1,2}\boldsymbol{x}_{12} \\ \boldsymbol{F}_{in2} = \boldsymbol{k}_{in2,1}\boldsymbol{x}_{in2} + \boldsymbol{k}_{in2,2}\boldsymbol{x}_{13} \\ \boldsymbol{F}_{in3} = \boldsymbol{k}_{in3,1}\boldsymbol{x}_{in3} + \boldsymbol{k}_{in3,2}\boldsymbol{x}_{14} \end{cases} \tag{32}$$

Based on Eq. (31) and Eq. (32), the output displacement $\boldsymbol{x}_{out}=[u,\ w,\ \theta]^{\mathrm{T}}$ of the central platform and the three input displacements $\boldsymbol{x}_{in1}$, $\boldsymbol{x}_{in2}$, $\boldsymbol{x}_{in3}$, can be analytically calculated as the explicit functions of the input actuating forces $\boldsymbol{F}_{p1}$, $\boldsymbol{F}_{p2}$, $\boldsymbol{F}_{p3}$

$$\begin{Bmatrix} \boldsymbol{x}_{in1} \\ \boldsymbol{x}_{in2} \\ \boldsymbol{x}_{in3} \end{Bmatrix} = \begin{bmatrix} \boldsymbol{f}_{11} & \boldsymbol{f}_{12} & \boldsymbol{f}_{13} \\ \boldsymbol{f}_{21} & \boldsymbol{f}_{22} & \boldsymbol{f}_{23} \\ \boldsymbol{f}_{31} & \boldsymbol{f}_{32} & \boldsymbol{f}_{33} \end{bmatrix} \cdot \begin{Bmatrix} \boldsymbol{F}_{p1} \\ \boldsymbol{F}_{p2} \\ \boldsymbol{F}_{p3} \end{Bmatrix} \tag{33}$$

$$\{\boldsymbol{x}_{out}\} = [\boldsymbol{g}_1 \quad \boldsymbol{g}_2 \quad \boldsymbol{g}_3] \cdot \begin{Bmatrix} \boldsymbol{F}_{p1} \\ \boldsymbol{F}_{p2} \\ \boldsymbol{F}_{p3} \end{Bmatrix} \tag{34}$$

where coefficients $\boldsymbol{f}_{ij}$ and $\boldsymbol{g}_i$ (i, j=1, 2, 3) describe the stiffness properties between the input/output displacements and the input actuating forces. These coefficients are all explicit functions of the elemental stiffness matrix of the compliant mechanism.

Also, the relationship between the output displacement and the input displacements can be further obtained by combining Eq. (33) with Eq. (34)

$$\{\boldsymbol{x}_{out}\} = \boldsymbol{J} \cdot \begin{Bmatrix} \boldsymbol{x}_{in1} \\ \boldsymbol{x}_{in2} \\ \boldsymbol{x}_{in3} \end{Bmatrix} = [\boldsymbol{g}_1 \quad \boldsymbol{g}_2 \quad \boldsymbol{g}_3] \begin{bmatrix} \boldsymbol{f}_{11} & \boldsymbol{f}_{12} & \boldsymbol{f}_{13} \\ \boldsymbol{f}_{21} & \boldsymbol{f}_{22} & \boldsymbol{f}_{23} \\ \boldsymbol{f}_{31} & \boldsymbol{f}_{32} & \boldsymbol{f}_{33} \end{bmatrix}^{-1} \cdot \begin{Bmatrix} \boldsymbol{x}_{in1} \\ \boldsymbol{x}_{in2} \\ \boldsymbol{x}_{in3} \end{Bmatrix} \tag{35}$$

where $\boldsymbol{J}$ denotes the Jacobian matrix of the compliant mechanism, which represents the kinematic relations between the input and the output displacements.

Here, the static model of the triangular lumped mass is conducted and other shapes of the platform, such as the rectangular platform that is also frequently used in multi-DOF flexible manipulators with rotational motion, can be considered with a similar procedure.

5. Summary of the modeling method

In Section 2, Section 3 and Section 4, three progressive kinematic/static modeling procedures are performed, respectively: (i) a general modeling method based on the displacement matrix method; (ii) condensed two-port mechanical network model for compliant mechanisms without rotational DOF; and (iii) the consideration of rotary motion as well as the condensed input/output force-displacement relations along with the Jacobian matrix for multi-DOF compliant mechanisms.

As a conclusion, the condensed two-port mechanical network model i.e. Eq. (21) is mainly used for compliant mechanisms with single input port-single output port (SISO); the input/output force-displacement relations i.e. Eq. (33) and Eq. (34) along with the Jacobian matrix i.e. Eq. (35) are built mainly for compliant mechanisms with multi input port-multi output port (MIMO) or multi input port-single output port (MISO). These models represent

the kinematic and static performances of a compliant mechanism from the perspective of input/output ports and are the explicit functions of the elemental stiffness matrices of the flexure hinge and the flexible beam or the equivalent condensed element. To obtain the expressions of these models, the matrix displacement method combined with the transfer matrix method is developed. The proposed modeling method is essentially a finite element method except for the following two improvements:

I) An analytically elemental stiffness matrix with high accuracy is deduced for all kinds of flexure hinges as a variable cross-section beam element. Therefore, the number of DOF is sharply reduced and the calculation efficiency is greatly improved compared to the usual FEM. So it can be regarded as a semi-analytical finite element method.

II) The transfer matrix method is flexibly combined with the displacement matrix method to simplify the modeling complexity of compliant mechanisms with serial-parallel substructures. Condensing the serial branch chains with the transfer matrix method and establishing the equilibrium equation of nodal force for parallel branch chains are easy operations owing to the utilization of the elemental stiffness matrix but not the compliance matrix in previous matrix-based methods [13, 14, 26-33].

The presented method has the advantages of conciseness and generality and also exhibits a good flexibility to complex compliant mechanisms with serial-parallel substructures. Moreover, the compliance of the flexure hinge and the flexible beam are both included to enhance the prediction accuracy of compliant mechanisms with distributed/hybrid compliance. For large deformation of compliant mechanisms, modified nonlinear or pseudo-rigid-body elemental stiffness matrix can be further built and included as a module into the modeling method, and the modeling procedure is still valid.

6. Verification and discussion

Two case studies were conducted to verify the presented method: (i) the first compares the presented method with the results from the commercial finite element software ANSYS and the experiment for the single-DOF compliant mechanism shown in Figure 1; (ii) the second application is an illustrative example of the multi-DOF compliant mechanism in Figure 7 performed to highlight how to consider a lumped mass with rotary motion and provide an investigation on the influence of the dimensions of the equivalent beam on the static performance.

6.1 Example one

(A) Finite element calculation by ANSYS

The compliant mechanism in Figure 1 was geometrically modeled by Pro/E software and the static analysis was carried out with the commercial finite element software package ANSYS. The Solid45 element was chosen to build the model and the local mesh was refined for the flexure hinges and the guiding beams. The results were proven to be convergent and accurate enough. An actuated force of 100 N was exerted on the bottom flexible beam. The material is Aluminium with density ρ=2770 kg/m^3, Young's modulus E=71 GPa and shear modulus G=27 GPa. The flexure hinges are circular with identical parameters. Minimum thickness and radius of the circular flexure hinges are, respectively, 0.5 mm and 1.25 mm. Width of the whole stage is 10 mm. Thickness of all the flexible beams except for the bottom one are 3 mm. Other necessary geometric parameters are shown in Figure 8 (a). Four simulation sets were carried out by selecting different thickness of the guiding beams while keeping other parameters constant. Detailed results of the displacement amplification ratio

and the input/output stiffness are comparatively listed in Table 1 and Table 2. Figure 8 (b) provides one result of the static deformation by FEM.

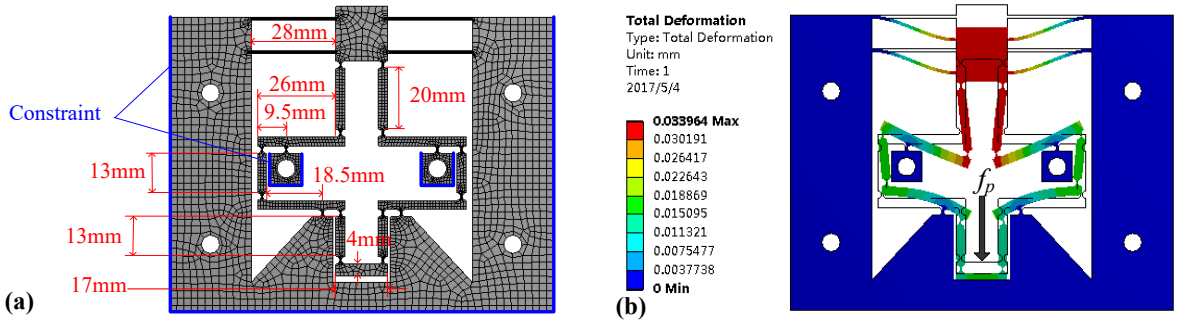

Figure 8 Finite elemental calculation. (a) Finite elemental model. (b) Result of one simulation set.

(B) Experiment

A monolithic prototype was fabricated with the guiding beam's thickness of 1 mm, while other material and geometric parameters are identical to the finite elemental model. The prototype and the experimental setup are shown in Figure 9. A piezo-actuator and its power amplifier from the Physik Instrumente Inc. were used as the motion generator. The piezo-actuator has a maximum output displacement of 15 μm at the driving voltage of 100 V. The fixed block of the compliant mechanism was mounted on an optical table to reduce the ground vibration. A real-time simulator with data acquisition system from the Henrun Inc. of China was used to analyze the measurement data. A laser displacement meter from KEYENCE with a 50 nm resolution was used to measure the output displacement. Up to 100 V non-negative sine voltages with 1 Hz were applied to the piezo-stacks. Figure 9 shows the experimental results of the output displacement versus the input voltage. In order to calculate the displacement amplification ratio, the following formula was adopted.

$$R = \frac{y_{out}}{K_v \cdot U \cdot K_P / (K_{in} + K_P)} \tag{36}$$

where y_{out} is the experimental output displacement. K_p=200 N/μm is the axial stiffness of the piezo-stacks. K_{in} is the input stiffness of the stage. K_v is the piezoelectric constant relating to the strain and is equal to 0.15 μm/V. U is the input voltage, V.

(C) Discussion

Table 1 and Table 2 compare the results of the displacement amplification ratio, the input and the output stiffness provided by the proposed model, four sets of FEM and experiment. Only one set of the displacement amplification ratio measured by the experiment is provided considering the high cost of the prototype. The displacement amplification ratio was calculated by dividing the output displacement by the input displacement under the actuating force of 100 N. The input and the output stiffness are the ratios of the input and output forces to their corresponding displacements. The analytical compliance matrix of the circular flexure hinge needed in the theoretical calculation is taken from [36].

The results show that the proposed method matches well with the results of FEM. The maximum deviation between the proposed method and FEM is less than 5% regarding the static displacement and less than 9% regarding the input and the output stiffness. It should be noted that the relative error of some simulation sets for the input and the output stiffness may large, but their absolute errors are small. In general, the prediction accuracy of the presented modeling method is satisfactory.

On the other hand, there is an approximately 8.5% drop in the measured results of the displacement amplification ratio in comparing the results of the theoretical model and FEM. The main error source may be the nonlinear deformation that was not considered in the theoretical and finite elemental models. Besides, the limited contact stiffness of Hertzian contact between the piezoelectric actuator and the compliant mechanism may slightly attenuate the stroke of the piezo-stacks in the experiment, resulting in some reduced output displacement of the compliant mechanism.

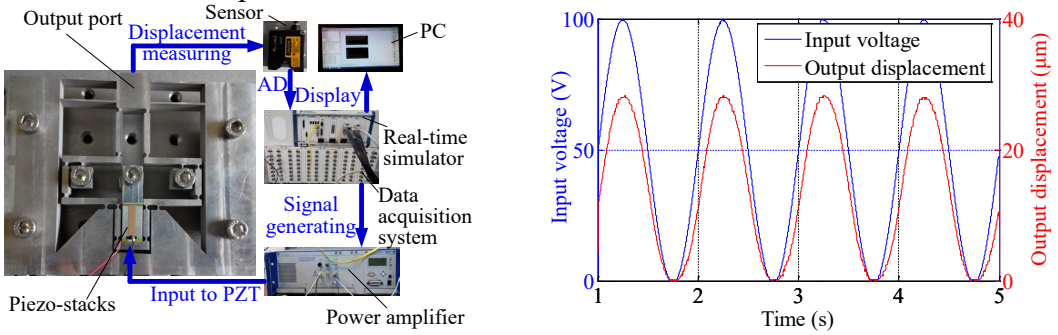

Figure 9 Prototype, experimental setup (left) and the measured results (right).

Table 1 Results of the displacement amplification ratio with different methods

Thickness of the guiding beam (mm)	The proposed method	FEM	Experiment	Error with FEM
0.2	3.08	3.00	——	0.08 (2.6%)
0.5	2.93	2.85	——	0.08 (2.8%)
1.0	2.13	2.13	1.95	0.00 (0.0%)
1.5	1.22	1.26	——	0.04 (3.2%)

Table 2 Results of the input and the output stiffness with different methods

Thickness of the guiding beam (mm)	K_{in} (N/μm)			K_{out} (N/μm)		
	The proposed method	FEM	Error	The proposed method	FEM	Error
0.2	5.08	5.49	0.41 (7.5%)	0.19	0.20	0.01 (5.0%)
0.5	5.22	5.61	0.39 (7.0%)	0.20	0.21	0.02 (9.0%)
1.0	5.92	6.30	0.38 (6.0%)	0.31	0.33	0.01 (6.1%)
1.5	6.72	6.82	0.10 (1.5%)	0.62	0.61	0.01 (1.6%)

6.2 Example two

The next numerical example is to calculate the static displacement of the multi-DOF compliant mechanism shown in Figure 6 (a) with the proposed modeling method and the finite element software package ANSYS. The detailed values for the geometric parameters defined in Figure 6 (b) are listed in Table 3. The elliptical flexure hinge with the theoretical compliance matrix in [36] is adopted again in this example and its geometric parameters are also listed in Table 3. The material in this example is kept to be the same as that in example one. Since the rotational angle of the platform can not be directly read from the results of FEM, the following formula is adopted to calculate the rotational angle of the platform under the load conditions of f_{p1}=f_{p2}=f_{p3}=100 N:

$$\theta = \arcsin\frac{\sqrt{u_{12}^2 + w_{12}^2}}{l_6} \tag{37}$$

where l_6=14.43 mm is defined in Figure 6 (b). u_{12} and w_{12} are, respectively, the output displacement of the node 12 in the x- and y- directions, which can be directly read from the FEM results.

Table 3 Key geometric and material parameters for FEM

Parameters	Values	Parameters	Values
h_1 (mm)	1.00	l_1 (mm)	12.00
h_2 (mm)	3.50	l_2 (mm)	5.00
h_e (mm)	0.50	l_3 (mm)	16.75
a (mm)	2.00	l_4 (mm)	20.00
b (mm)	1.25	l_5 (mm)	25.00
w (mm)	10.00	l_6 (mm)	14.43

Figure 10 shows the total displacement distributions of the compliant mechanism by FEM when two sets of the load conditions are performed. Detailed results of the input and the output displacements obtained from the FEM are comparatively listed in Table 4 with those obtained from the proposed model. During the theoretical calculation, the thickness of the equivalent beams for simulating the platform with lumped mass was set as 5 mm. From the results in Table 4, one can see that the theoretical results are comparable with the FEM results and the maximum deviation is less than 10% in a large range except for the prediction error of the rotational angle is 13%. The reason of the larger deviation in the rotational angle's result may be that an approximate model, i.e. Eq. (37), was adopted to indirectly calculate its value for FEM, which may brings about some errors. As a conclusion, the proposed modeling method can analytically predict the static performance of the multi-DOF compliant mechanism with an acceptable accuracy.

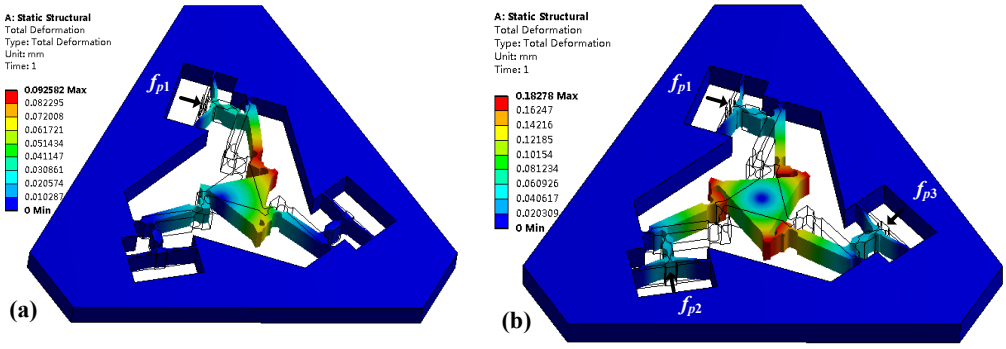

Figure 10 Finite element results. (a) f_{p1}=100 N, f_{p2}=f_{p3}=0 N. (b) f_{p1}=f_{p2}=f_{p3}=100 N.

Table 4 Results of the input and the output displacement with different methods

Method	f_{p1}=100 N, f_{p2}=f_{p3}=0 N			f_{p1}=f_{p2}=f_{p3}=100 N							
	x_{in1} (μm)	x_o (μm)		x_{in1} (μm)	x_{in2} (μm)		x_{in3} (μm)		x_o (μm/rad)		
	u	u	w	u	u	w	u	w	u	w	θ
FEM	29.4	26.7	-11.0	42.4	-21.3	36.8	-21.3	-36.7	0	0	0.0115
The proposed method	29.6	28.1	-11.4	46.3	-23.1	40.1	-23.2	-40.1	0	0	0.0130
Error	0.7%	5.2%	3.6%	9.2%	8.5%	9.0%	8.9%	9.3%	0	0	13%

Noting: u and w denote the displacement components in the x- and y- directions. θ is the rotary angle of the platform.

The platform of compliant mechanisms with rotational motion is simplified as a series of equivalent beams in the proposed modeling method to deal with the rotary DOF. To illustrate the influence of the thickness of the equivalent beams on the static performance, the three input displacement components in the x direction were calculated with the change of the thickness of the equivalent beams while keeping other geometric parameters constant, as shown in Table 3. The calculated results are shown in Figure 11. During the analysis, f_{p1}=f_{p2}=f_{p3}=100 N were exerted on the three input ports. One can see that the results begin to converge and become stationary after the threshold of about 3 mm under the given geometric

parameters. The results mean that the thicker the equivalent beams, the higher accuracy of the presented modeling method.

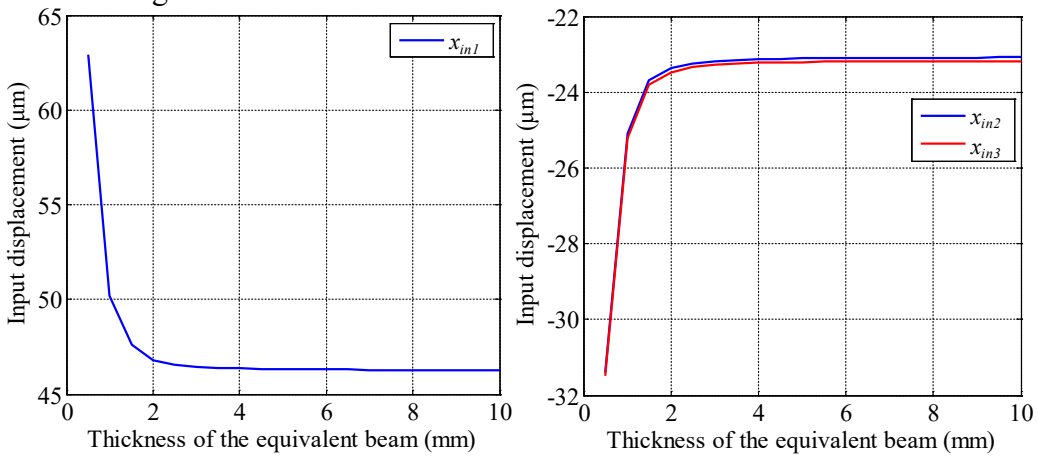

Figure 11 Influence of the thickness of the equivalent beams on the static performance.

7. Conclusions

A general and accurate modeling methodology is proposed for analyzing the kinematic and static performance of complex compliant mechanisms with serial-parallel substructures and distributed/hybrid compliance. First, a semi-analytical finite element model is proposed based on the displacement matrix method. Second, the transfer matrix method is flexibly combined with the displacement matrix method to condense the serial-parallel branch chains and then a two-port mechanical network model is established for single-DOF compliant mechanisms. Lastly, how to deal with the issue of rotational motion in multi-DOF compliant mechanisms is carried out and the input/output force-displacement relations along with the Jacobian matrix are further established from the viewpoint of input and output ports. The compliance of the flexure hinge and the flexible beam are both included in the presented model to enhance the prediction accuracy of distributed compliant mechanisms. Two examples, including a single-DOF compliant mechanism and a multi-DOF XYθ precision positioning stage, are carried out to verify the proposed approach, and the results are in agreement with those from FEM and experiment.

Acknowledgment

This work was supported by the National Natural Science Foundation of China (grant numbers 51705487, 51575426), China; and the State Key Laboratory Program of Xi'an Jiaotong University (grant number SV2016-KF-19), China.

Appendix A:

Eq.(4) is the compliance matrix of a planar flexure hinge. Its expression is as follows [35-38]

$$c_x = \int_0^{l_i} \frac{1}{EA(x)}dx,\ c_y = \int_0^{l_i} \frac{x^2}{EI(x)}dx$$
$$c_\theta = \int_0^{l_i} \frac{1}{EI(x)}dx,\ c_\alpha = -\int_0^{l_i} \frac{x}{EI(x)}dx \quad \text{(A.1)}$$

As shown in Fig. 4, the *i*th flexure hinge has only three independent nodal forces, thus

$$\begin{Bmatrix} F_{jx} & F_{jy} & M_j & F_{kx} & F_{ky} & M_k \end{Bmatrix}^{\mathrm{T}} = \begin{bmatrix} 1 & 0 & 0 & -1 & 0 & 0 \\ 0 & 1 & 0 & 0 & -1 & l_i \\ 0 & 0 & 1 & 0 & 0 & 1 \end{bmatrix}^{\mathrm{T}} \cdot \begin{Bmatrix} F_{jx} \\ F_{yj} \\ M_j \end{Bmatrix} \tag{A.2}$$

Based on the elastic beam theory, the translational and rotational displacements can be expressed as

$$\begin{cases} u_k = \int_0^{l_i} \dfrac{F_k}{EA(x)} dx + u_j \\ \theta_k = \int_0^{l_i} \dfrac{M_j - F_{yj} \cdot x}{EI(x)} dx + \theta_j \\ w_k = \int_0^{l_i} \int \dfrac{M_j - F_{yj} \cdot x}{EI(x)} dx dx + \theta_j l_i + w_j \end{cases} \tag{A.3}$$

By substituting Eq. (A.1) into Eq. (A.3), and then substitute the result into Eq. (A.2), the elemental stiffness matrix of the *i*th flexure hinge can be ultimately deduced by using relationship, k_y=-2k_α/l_i [40], as

$$\begin{Bmatrix} F_{jx} \\ F_{jy} \\ M_j \\ F_{kx} \\ F_{ky} \\ M_k \end{Bmatrix} = \begin{bmatrix} k_x & 0 & 0 & -k_x & 0 & 0 \\ & k_y & -k_\alpha & 0 & -k_y & -k_\alpha \\ & & k_\theta & 0 & k_\alpha & -l_i \cdot k_\alpha - k_\theta \\ & & & k_x & 0 & 0 \\ & Sym & & & k_y & k_\alpha \\ & & & & & k_\theta \end{bmatrix} \cdot \begin{Bmatrix} u_j \\ w_j \\ \theta_j \\ u_k \\ w_k \\ \theta_k \end{Bmatrix} \tag{A.4}$$

References

[1] Howell L L. Compliant mechanisms[M]. John Wiley & Sons, 2001.

[2] Yong Y K. A new preload mechanism for a high-speed piezoelectric stack nanopositioner[J]. Mechatronics, 2016, 36: 159-166.

[3] Noveanu S, Lobontiu N, Lazaro J, et al. Substructure compliance matrix model of planar branched flexure-hinge mechanisms: Design, testing and characterization of a gripper[J]. Mechanism and Machine Theory, 2015, 91: 1-20.

[4] Hao G, Yu J. Design, modelling and analysis of a completely-decoupled XY compliant parallel manipulator[J]. Mechanism and Machine Theory, 2016, 102: 179-195.

[5] Ueda J, Secord T W, Asada H H. Large effective-strain piezoelectric actuators using nested cellular architecture with exponential strain amplification mechanisms[J]. IEEE/ASME Transactions on Mechatronics, 2010, 15(5): 770-782.

[6] Lan C C, Lee K M. Generalized shooting method for analyzing compliant mechanisms with curved members[J]. Journal of Mechanical Design, 2006, 128(4): 765-775.

[7] Yong Y K, Lu T F, Handley D C. Review of circular flexure hinge design equations and derivation of empirical formulations[J]. Precision engineering, 2008, 32(2): 63-70.

[8] Lobontiu N, Garcia E. Analytical model of displacement amplification and stiffness optimization for a class of flexure-based compliant mechanisms[J]. Computers & structures, 2003, 81(32): 2797-2810.

[9] Ling M, Cao J, Zeng M, et al. Enhanced mathematical modeling of the displacement amplification ratio for piezoelectric compliant mechanisms[J]. Smart Materials and Structures, 2016, 25(7): 75022-75032.

[10] Choi K B, Lee J J, Kim G H, et al. Amplification ratio analysis of a bridge-type

mechanical amplification mechanism based on a fully compliant model[J]. Mechanism and Machine Theory, 2018, 121: 355-372.
[11] Park S R, Yang S H. A mathematical approach for analyzing ultra precision positioning system with compliant mechanism[J]. Journal of Materials Processing Technology, 2005, 164: 1584-1589.
[12] Wadikhaye S. Design, characterization and control of serial-kinematic XYZ nanopositioner for high-speed Atomic Force Microscopy[J]. 2014.
[13] Xiao S, Li Y. Optimal Design, Fabrication, and Control of an $ XY $ Micropositioning Stage Driven by Electromagnetic Actuators[J]. IEEE transactions on Industrial Electronics, 2013, 60(10): 4613-4626.
[14] Choi S B, Han S S, Han Y M, et al. A magnification device for precision mechanisms featuring piezoactuators and flexure hinges: Design and experimental validation[J]. Mechanism and Machine Theory, 2007, 42(9): 1184-1198.
[15] Howell L L, Midha A. A method for the design of compliant mechanisms with small-length flexural pivots[J]. Journal of mechanical design, 1994, 116(1): 280-290.
[16] Venkiteswaran V K, Su H J. Pseudo-rigid-body models for circular beams under combined tip loads[J]. Mechanism and Machine Theory, 2016, 106: 80-93.
[17] Zhang A, Chen G. A comprehensive elliptic integral solution to the large deflection problems of thin beams in compliant mechanisms[J]. Journal of Mechanisms and Robotics, 2013, 5(2): 021006.
[18] Zubir M N M, Shirinzadeh B, Tian Y. A new design of piezoelectric driven compliant-based microgripper for micromanipulation[J]. Mechanism and Machine Theory, 2009, 44(12): 2248-2264.
[19] Pham H H, Chen I M. Kinematics, workspace and static analyses of 2-DOF flexure parallel mechanism[C]//Control, Automation, Robotics and Vision, 2002. ICARCV 2002. 7th International Conference on. IEEE, 2002, 2: 968-973.
[20] Ma H W, Yao S M, Wang L Q, et al. Analysis of the displacement amplification ratio of bridge-type flexure hinge[J]. Sensors and Actuators A: Physical, 2006, 132(2): 730-736.
[21] Li Y, Xu Q. Development and assessment of a novel decoupled XY parallel micropositioning platform[J]. IEEE/Asme Transactions On Mechatronics, 2010, 15(1): 125-135.
[22] Mottard P, St-Amant Y. Analysis of flexural hinge orientation for amplified piezo-driven actuators[J]. Smart Materials and Structures, 2009, 18(3): 035005.
[23] Qi K, Xiang Y, Fang C, et al. Analysis of the displacement amplification ratio of bridge-type mechanism[J]. Mechanism and Machine Theory, 2015, 87: 45-56.
[24] Ling M, Cao J, Jiang Z, et al. Theoretical modeling of attenuated displacement amplification for multistage compliant mechanism and its application[J]. Sensors and Actuators A: Physical, 2016, 249: 15-22.
[25] Zhu X, Xu X, Wen Z, et al. A novel flexure-based vertical nanopositioning stage with large travel range[J]. Review of Scientific Instruments, 2015, 86(10): 105112.
[26] Koseki Y, Tanikawa T, Koyachi N, et al. Kinematic analysis of a translational 3-dof micro-parallel mechanism using the matrix method[J]. Advanced Robotics, 2002, 16(3): 251-264.
[27] Liu P, Yan P, Zhang Z. Design and analysis of an X–Y parallel nanopositioner supporting large-stroke servomechanism[J]. Proceedings of the Institution of Mechanical Engineers, Part C: Journal of Mechanical Engineering Science, 2015, 229(2): 364-376.
[28] Pham H H, Chen I M. Stiffness modeling of flexure parallel mechanism[J]. Precision

Engineering, 2005, 29(4): 467-478.
[29] Lobontiu N. Compliance-based matrix method for modeling the quasi-static response of planar serial flexure-hinge mechanisms[J]. Precision Engineering, 2014, 38(3): 639-650.
[30] Jiang Y, Li T M, Wang L P. Stiffness modeling of compliant parallel mechanisms and applications in the performance analysis of a decoupled parallel compliant stage[J]. Review of Scientific Instruments, 2015, 86(9): 095109.
[31] Ryu J W, Lee S Q, Gweon D G, et al. Inverse kinematic modeling of a coupled flexure hinge mechanism[J]. Mechatronics, 1999, 9(6): 657-674.
[32] Kim J J, Choi Y M, Ahn D, et al. A millimeter-range flexure-based nano-positioning stage using a self-guided displacement amplification mechanism[J]. Mechanism and Machine Theory, 2012, 50: 109-120.
[33] Lai L J, Zhu Z N. Design, modeling and testing of a novel flexure-based displacement amplification mechanism[J]. Sensors and Actuators A: Physical, 2017, 266: 122-129.
[34] Awtar S, Sen S. A generalized constraint model for two-dimensional beam flexures: nonlinear load-displacement formulation[J]. Journal of Mechanical Design, 2010, 132(8): 081008.
[35] Tseytlin Y M. Notch flexure hinges: an effective theory[J]. Review of Scientific Instruments, 2002, 73(9): 3363-3368.
[36] Chen G, Ma Y, Li J. A tensural displacement amplifier employing elliptic-arc flexure hinges[J]. Sensors and Actuators A: Physical, 2016, 247: 307-315.
[37] Meng Q, Li Y, Xu J. New empirical stiffness equations for corner-filleted flexure hinges[J]. Mechanical Sciences, 2013, 4(2): 345-356..
[38] Li T M, Zhang J L, Jiang Y. Derivation of empirical compliance equations for circular flexure hinge considering the effect of stress concentration[J]. International Journal of Precision Engineering and Manufacturing, 2015, 16(8): 1735-1743.
[39] Yi B J, Chung G B, Na H Y, et al. Design and experiment of a 3-DOF parallel micromechanism utilizing flexure hinges[J]. IEEE Transactions on Robotics and Automation, 2003, 19(4): 604-612.
[40] Lobontiu N. Note: Bending compliances of generalized symmetric notch flexure hinges[J]. Review of Scientific Instruments, 2012, 83(1): 016107.